Plasma Processes and Polymers

PLASMA PROCESSES AND POLYMERS

RESEARCH ARTICLE OPEN ACCESS

Bubbling Water-Treating DBD Plasma Device Optimization Using Experimental and Computational Methods

Conner D. Robinson | Nicholas L. Sponsel | Katharina Stapelmann

Department of Nuclear Engineering, North Carolina State University, Raleigh, North Carolina, USA

Correspondence: Katharina Stapelmann (kstapel@ncsu.edu)

Received: 19 November 2024 | **Revised:** 7 January 2025 | **Accepted:** 23 January 2025

Keywords: dielectric barrier discharges (DBD) | modeling | non-thermal plasma (NTP) | plasma treated water (PTW)

ABSTRACT

A dry air atmospheric pressure volume dielectric barrier discharge is employed to fix nitrogen in water. Producing nitrate for use as nitrogen fertilizer is the primary motivation. A 0D chemistry model is developed and informed by the electrical, and geometric characteristics of the device and the plasma gas temperature. Modeled ozone and nitrate densities are compared to those measured experimentally in the plasma effluent and treated liquid for a range of gas temperatures. Modeled and measured ozone densities are in good agreement; however, the model lacks the liquid chemistry to properly represent the measured nitrate density. A gas temperature-based shift from ozone to NO_x producing regimes is observed in both experiment and model, and the reactions responsible are evaluated.

1 | Introduction

In modernity, the production of nitrogen-based fertilizers has been enabled by the Haber-Bosch process. While this is an efficient process, much of the nitrogen content of the fertilizer is lost to the environment via ammonia volatilization, denitrification, and leaching [1, 2]. This leads to the production of greenhouse gases and the toxification of groundwater [3, 4]. It is also an energy-intensive process, requiring high temperatures (700 K) and pressures (100 atm), which can only be obtained in large-scale industrial facilities [5]. Transportation from factory to farm incurs an additional environmental impact, and limits availability. Atmospheric pressure plasma treatment of water, as an alternative to the Haber-Bosch process, has the potential to significantly reduce the environmental impact of producing nitrogen fertilizer. In this study, we attempt to improve these methods by optimizing the generation and transport of relevant chemical species - nitrate - using a water-treating plasma device.

Numerous applicable chemicals can be produced by atmospheric pressure air plasmas, such as nitrite (NO_2^-), nitrate (NO_3^-), ammonium (NH_4^+), and hydrogen peroxide (H_2O_2). By producing a plasma in close proximity to water, these species can be fixed in the liquid. Plasma treated water (PTW, sometimes referred to as plasma activated water (PAW)) has been shown to be an effective substitute for off-shelf nitrogen-based fertilizers [5–9].

Many types of plasma devices have been developed to treat water [10]. Recently, efforts on scaling and efficiency were reviewed in [11]. One of the simplest is a surface treating dielectric barrier discharge (DBD), wherein the water is suspended between two parallel plate electrodes, and the plasma is generated in a volume just above the water's surface [12, 13]. These designs often use a directional flow of feed gas to promote the transport of the produced reactive oxygen and nitrogen species (RONS) to the liquid, improving efficiency—commonly seen in plasma jets [9, 14–19]. By encasing the electrode in a gas-flowing nozzle and submerging the end, the plasma effluent

can be forced into the liquid as bubbles, further improving RONS transport [20–22]. This often results in plasma generation within the bubbles themselves, which creates significantly different chemistry due to the higher humidity in the gas and proximity of the water surface [20, 23].

In this study, we use a bubbling DBD based on a device which produced almost exclusively nitrate, as per a study by Tachibana et al. [10], the "water-sealed DBD" or WS-DBD. Before the work shown here, the geometry of this device was optimized for nitrate production based on the plasma residence time of the feed gas and the bubble transport parameters. The results of this optimization are discussed in the supplementary materials.

To improve the applicability of plasma treatment for nitrogen fertilizer, it is important to understand the mechanisms responsible for the generation of RONS such that they can be optimized. To that end, a 0D model of the gas phase chemistry was created using the Zapdos framework [24]. Modeled results are compared to experimental ones made using the aforementioned bubbling DBD plasma device. For this comparison, we optically measure the gas temperature and ozone density in the plasma effluent. Liquid phase concentrations of nitrate are also determined colorimetrically post-treatment. Current and voltage measurements are made to determine deposited power, number of plasma events, and average power per event. Gas temperature is a dominant factor governing the reactions within the 0D model and is therefore the primary variable used for this comparison. Experimentally, the plasma gas temperature is modulated by adjusting the applied voltage and frequency of the power supply. Good agreement between model and experiment was observed, and the significance of gas temperature in governing the reaction pathways is discussed.

2 | Materials and Methods

2.1 | Plasma Device

The volume DBD used here, depicted in Figure 1, is largely defined by the separation of the plasma volume and the water body above, into which the plasma effluent flows. This is achieved by joining a sealed, 3D-printed plasma chamber to a PVC tube, with a thin stainless steel filter between to prevent the water from flowing down and into the plasma chamber.

There is a 2 mm gap between the top (grounded) electrode and the dielectric covering the bottom (powered) electrode, wherein the plasma is generated. The powered electrode is a copper pipe end cap (radius = 29 mm). The grounded electrode is a 1 cm thick stainless steel plate, well exceeding the size of the powered electrode (7 cm^2). A 0.5 mm thick alumina (Al_2O_3) ceramic sheet separates the powered electrode from the plasma volume. These pieces are assembled within a 3D-printed resin housing, with quartz glass windows on two opposing sides to allow optical access to the plasma. Dry air is flowed in from the side of the chamber and allowed to vent out through a hole located in the center of the grounded electrode, up through a stainless steel sparger nozzle (McMaster-Carr 8226T13), and into the water above. Airflow is controlled by a mass flow controller

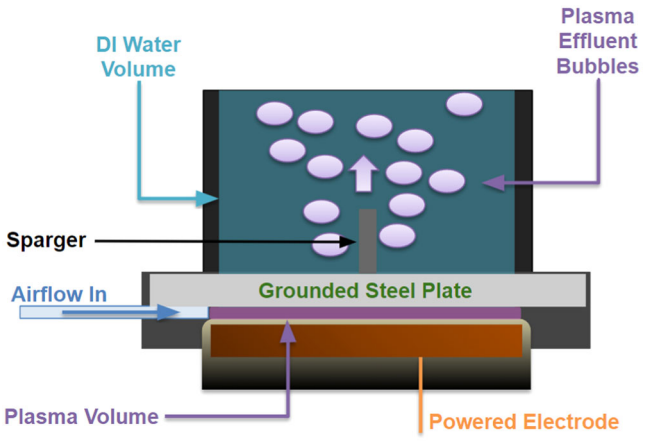

FIGURE 1 | The plasma device used here is a parallel plate dielectric barrier discharge (DBD). This was originally based on the water-sealed design discussed in [10]. The plasma occurs in a sealed volume, ensuring the plasma effluent is forced into the water contained above. The sparger prevents the water from back-flowing into the plasma chamber and diffuses the plasma effluent into small bubbles, improving RONS transport into the liquid.

(Alicat, MC-5SLPM-D-PCV30/5M) and kept at 1000 sccm. The powered electrode is fan-cooled from below to prevent the 3D-printed material of the housing from overheating. For the experimental results shown here, 200 mL of deionized water is treated.

The applied frequency and voltage to the plasma were controlled with an arbitrary function generator (Tektronix, AFG3052C). This function generator was used to supply a sinusoidal waveform to a high-voltage amplifier (Matsusada Precision Inc., AMP-20B20), wherein the signal was amplified before being sent on to the plasma device. For the results shown here, the frequency and voltage were varied from 400 to 2400 Hz and 22–39.1 kV_{pp}; however, due to the power limitations of the power supply, the frequency range is reduced for higher voltages.

2.2 | Electrical Diagnostics

Current and voltage measurements were taken using a current monitor (Pearson Electronics, Model 6585) and voltage probe (North Star, PVM-4), whose outputs were collected using a digital oscilloscope (Tektronix, MDO3104), see Figure 2. Power is derived from these measurements using an equivalent circuit model. Power is determined following [25], using:

$$P_P(t) = I_{p,g}(t) \times U_g(t) \quad (1)$$

where $U_g(t)$ and $I_{p,g}$ are the gap voltage and current.

Averaged measurements of the current/voltage were taken using the oscilloscope's internal averaging function, set to collect 512 samples per measurement. These were used for the power calculations as they tended to provide more reliable results than single-shot measurements due to the filamentary nature of the plasma.

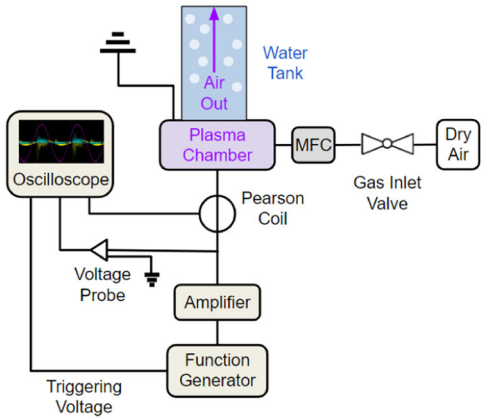

FIGURE 2 | Simplified diagram of the power supply and electrical diagnostics used with the plasma device. A triggering voltage was sent to the oscilloscope for multi-sample averaged measurements.

2.3 | Optical Diagnostics

A series of optical diagnostics were performed on the plasma, plasma effluent, and samples of the plasma-treated water, described in the following sections.

2.3.1 | Gas Temperature

Optical emission spectroscopy is performed to determine the plasma gas temperature (T_g) [26]. Gas temperature has a significant impact on chemical reaction rates, making it vital for comparisons between the experimental results and the 0D model. To determine the gas temperature, the rotational distribution of the emission spectrum of the second positive molecular bands of nitrogen ($N_2(C^3\Pi_g \rightarrow B^3\Pi_u, 0-0)$) are observed. Equilibrium between the translational and rotational degrees of freedom of the ground state nitrogen molecules is assumed due to rotational relaxation in atmospheric pressure plasmas. Electron impact excitations are limited by the selection rule $\Delta J = 0, \pm 1$; thus, the rotational distributions are approximately equivalent between the ground and excited states of the nitrogen molecule. The temperature is determined by fitting the measured spectra to a simulated one. Using this method, we achieve an uncertainty of ± 10 K.

The emission spectra of the DBD are measured using an Echelle spectrometer (ESA 4000plus, LLA Instruments). The echelle spectrometer features a wide spectral range between 200 and 800 nm and a unique wavelength-dependent resolution. The resulting FWHM resolution of the spectrometer ranges from ~15 pm at 200 nm to ~60 pm at 800 nm with an attendant pixel resolution of 5 pm at 200 nm and 20 pm at 800 nm. This spectrometer was relatively and absolutely calibrated using a calibrated tungsten ribbon lamp in conjunction with a deuterium lamp, following [27].

2.3.2 | Ozone Densities in the Effluent

Optical absorption spectroscopy (OAS) was performed on the plasma effluent just as it exited the plasma chamber, approximately 1.5 cm above the grounded plate (with the sparger and water tank removed) to determine ozone densities. Absorbance values were obtained using an UV-VIS-NIR light source (Ocean Optics DH-2000-BAL) in conjunction with a spectrometer (Ocean Optics QE65 Pro) and a cuvette holder (Ocean Optics CUV-UV). The measured absorbances can be directly interpreted as densities based on the Beer–Lambert Law:

$$A = \log\frac{I}{I_0} = \varepsilon \ell c \tag{2}$$

where A is the absorbance, I is the measured intensity of light at a given wavelength, I_0 is the intensity of light without the absorbing medium (gaseous ozone for our purpose), ε is the absorption cross-section for the absorbing medium, ℓ is the path length of light through the absorbing medium (1 cm here), and c is the density of the absorbing medium. Here we take ε to be 1.11×10^{-17} cm^2 molecule^{-1} at 255 nm [28].

2.3.3 | Liquid Phase Densities

To determine densities of relevant RONS in the liquid phase, colorimetry was performed on liquid samples after 20 min of continuous plasma treatment of 200 ml of deionized water for the entire voltage-frequency parameter space. In all cases, NO_3^-, NO_2^-, H_2O_2, and NH_4^+ were tested for using the commercially available Supelco test kits: 1.09713, 1.14776, 1.18789, and 1.14752, respectively.

The same Ocean Optics equipment as described above was used for aqueous phase absorption measurements. At least 20 min elapsed between end of treatment and measurement. Despite the constant turbulence in the liquid column caused by the flowing bubbles, varying concentrations had been observed for samples taken from different depths in the liquid column. Therefore, before sampling, the entire treated volume of liquid was removed from the device and thoroughly mixed to ensure the measured density was not influenced by any spatial gradients in the liquid. Measured absorbances were compared with standard curve values (acquired from stock solutions) to obtain concentrations. Of the four species tested, only NO_3^- was ever observed. Given the absence of humidity in the feed gas, the lack of H_2O_2, and NH_4^+ is expected. NO_2^- also tends to react into other species, including NO_3^-, over longer time scales [10, 29–31].

2.4 | Plasma Chemistry Model

The concept of modeling the chemistry of atmospheric air discharge in the presence of water is not a new one [32]. The intention behind the use of one here is to tailor it to our specific case, to gain a better understanding of the relevant chemical reactions for this plasma device. Ideally, the results of which will aid in the improvement of this device and similar PTW-producing volume DBDs.

To wit, a 0D chemistry model of the plasma and effluent was created using the Zapdos application. Zapdos is an open-source

finite element plasma fluid solver based on the Multiphysics Object Oriented Simulation Environment (MOOSE) framework [24, 33, 34]. Zapdos is coupled with CRANE, a chemical reaction network solver, and the primary feature utilized here. The reaction network includes 530 reactions and 35 species, see Table 1.

This model is intended to portray the average chemical density of the effluent as it exists the plasma chamber, with the final time step (and the time of the results presented below) corresponding to approximately the time at which the effluent reaches the liquid interface, just beyond the sparger nozzle. A background gas of 79% N_2 and 21% O_2 is used to mimic the composition of air used in the experiment. The initial electron density is set to 1×10^{14} cm^{-3} with an equal number of positive ions (90% N_2^+ and 10% O_2^+). A ten nanosecond voltage pulse - a simple spike with 5 ns rise and fall periods peaking at 9.5 kV - is used to model a plasma filament. This is approximately the time span of the measured current spikes and this particular voltage was chosen to match the power deposited into the electrons in the model, with that of the measured power of a single current spike. The average power of a single current spike is determined by integrating the product of plasma current and voltage and is approximately 0.316 mJ on average.

Following this pulse, the voltage is reduced to zero and the chemistry is allowed to evolve until $t = 0.166$ s, where the model ends. This is the estimated average time between the plasma filament and the plasma effluent reaching the liquid interface at the edge of the sparger. The ozone density measurements are made in approximately the same location, to align with this timing of the 0D model. The time step increases incrementally by 1% over the course of the simulation from 1×10^{-12} s to a maximum of 1×10^{-3} s. This simulation is performed for a range of gas temperatures from 320 to 560 K (which are held constant for the entire run time), with 20 K increments.

The majority of the electron impact reactions are the functional forms provided by Sakiyama et al. [35]. These are partly supplemented with those offered by [36] using corresponding cross-sections from the Phelps database [37]. General reaction rates were assembled from [35, 36, 38]. Ion recombination reactions are based on the schemes provided by [38]. Water/hydrogen species were not included due to the feed gas being comprised of dry air and the active plasma region's separation from the water being treated.

3 | Results and Discussion

3.1 | Experimental Results

3.1.1 | Electrical Diagnostics

Current and voltage were measured for the entire voltage-frequency space. An example of the measured waveforms for a single period is depicted in Figure 3. Using the current/voltage measurements and the method previously described the plasma power is determined. As one might expect, there is a strong linear relation of plasma power with both frequency and voltage (see Figure 4). Due to limitations of the used amplifier, not all amplitude and frequency combinations were possible.

The number of plasma events was also counted, taking these to be spikes in current [39–43]. This is used to estimate the number of plasma filaments which occur in a given volume of air, as it travels through the plasma. Filaments may occur sufficiently close together (in time) such that they cannot be distinguished in the current measurement, so this value is an approximation. This number varies with applied frequency and voltage from 70,000–210,000 filaments per second. Taking the plasma region to have the same area as the powered electrode (2.64 cm^2) and the cross-sectional area of a filament to be 0.0314 mm^2 (a circle with radius = 0.1 mm) then the average filament

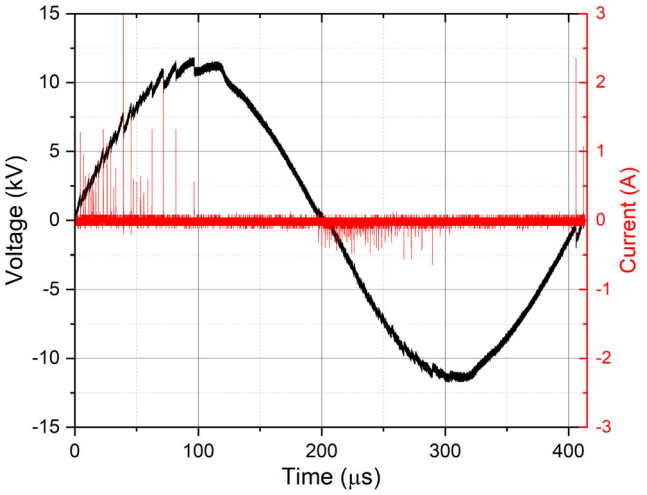

FIGURE 3 | Example of measured current and voltage waveform for a single voltage period at 2400 Hz. Spikes in plasma current are indicative of plasma events [39–43]. These spikes are used to determine the average number of plasma events occurring in the plasma volume.

TABLE 1 | Chemical species included in the 0D plasma model. 12 neutral species, 4 excited state species, and 18 ionic species are included. Water and hydrogenated species are not included due to the absence of water in the feed gas, and the separation between the liquid volume and the plasma chamber.

Ground state neutrals	Excited neutrals	Charged species
N, N_2,	$N(^2D)$, $N_2(A\,^3\Sigma_u^+)$	N^+, N_2^+, N_3^+, N_4^+
O, O_2, O_3	$O(^1D)$, $O_2(a^1\Delta_g)$	O^+, O^-, O_2^+, O_3^+, O_3^-, O_4^+, O_4^-
NO, NO_2, NO_3		NO^+, NO^-, NO_2^+, NO_2^-, NO_3^-
N_2O, N_2O_3, N_2O_4, N_2O_5		N_2O^+, N_2O^-

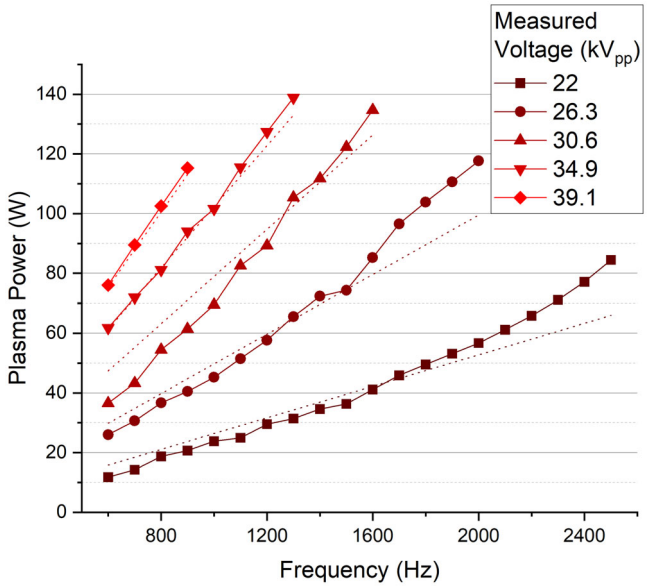

FIGURE 4 | Plasma power, P_P, calculated from the measured current and voltage. Power linearly increases with both frequency and voltage as one would expect.

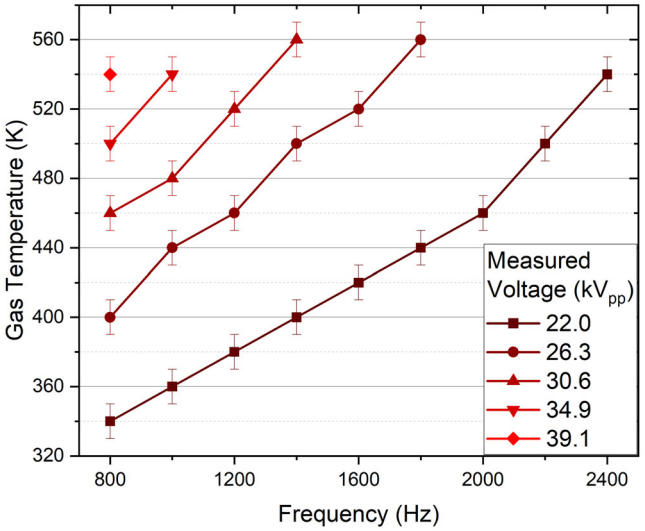

FIGURE 5 | Gas temperature results from OES spectra of the N_2 (C–B, 0–0) rotational band. The error of ±10 K is a product of the fitting procedure. Comparing the experimental and model results utilize the gas temperatures as presented here.

density per second is 0.825–2.475. The refresh rate of the air within the plasma volume can be estimated as:

$$t_{\text{ref}} = \frac{V_P}{Q} = 0.31704 \text{ s} \tag{3}$$

where V_P is the plasma volume (5285 mm^3) and Q is the airflow rate. Taking this to be the average amount of time a given volume of air resides within the plasma, then this volume sees 0.262–0.785 filaments on average. This is important for how it relates to the 0D model, the results of which are discussed in the chemistry model results section. Only a single pulse is simulated in our model; which is sufficient according to this approximation.

3.1.2 | Gas Temperature

OES measurements indicate gas temperatures from 340 to 560 K over the frequency-voltage space (Figure 5). Generally, the simulated spectra were able to obtain good fits to the measured spectra (Figure 6). These results are well within the expected range of a volume DBD operated in air [44, 45].

3.1.3 | Species Densities

Results from the liquid phase measurements of nitrate are shown below in Figure 7 as production $P_{NO_3^-}$ (mg/min):

$$P_{NO_3^-} = \frac{C_{NO_3^-} V_{\text{liq}}}{t} \tag{4}$$

where $C_{NO_3^-}$ is the measured concentration, V_{liq} is the volume of treated water (200 ml) and t is the treatment time (20 min). The

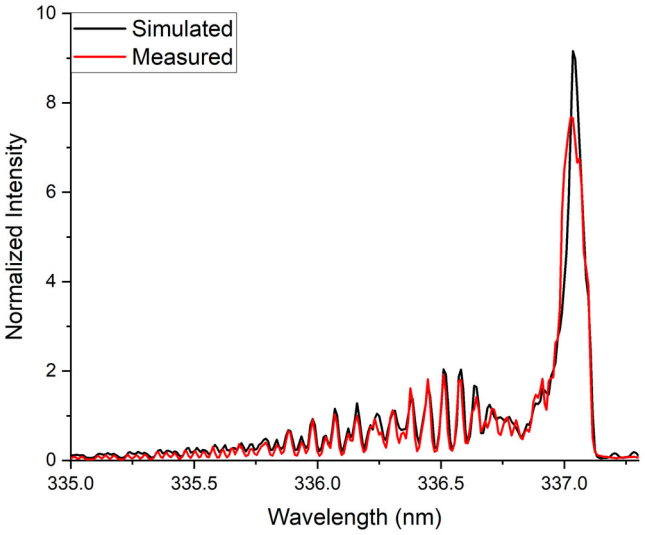

FIGURE 6 | Measured and simulated spectra of the plasma volume. Example fit of the C–B (0–0) rotational band for the 22 kV_{pp}, 800 Hz case, with a fit temperature of 340 K.

other species we tested for (NO_2^-, NH_4^+ and H_2O_2) were never detected. While varying voltage/frequency of the plasma, it is observed that the rate of production largely trends with gas temperature. Nitrate production increases with gas temperature from 340 K to 420 K before leveling off and eventually decreasing above 500 K.

The results of the OAS measurements of ozone in the plasma effluent can be seen in Figure 7 as well, given in number density. It too demonstrates a strong dependence on the gas temperature of the plasma; initially high at high gas temperatures, and decreasing to below detectable levels by 460 K, also known as "discharge poisoning" [46].

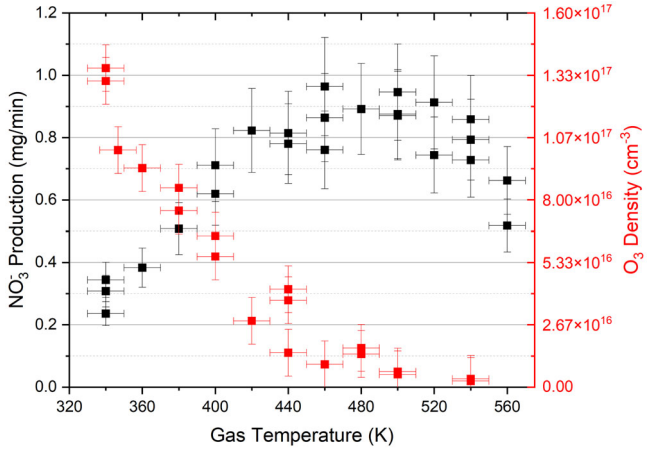

FIGURE 7 | Measured nitrate production and ozone density as a function of gas temperature. Ozone is initially high at low temperatures, before quickly decreasing below the detection limit. Nitrate seems to follow an inverse trend, before eventually leveling off and decreasing at high gas temperatures.

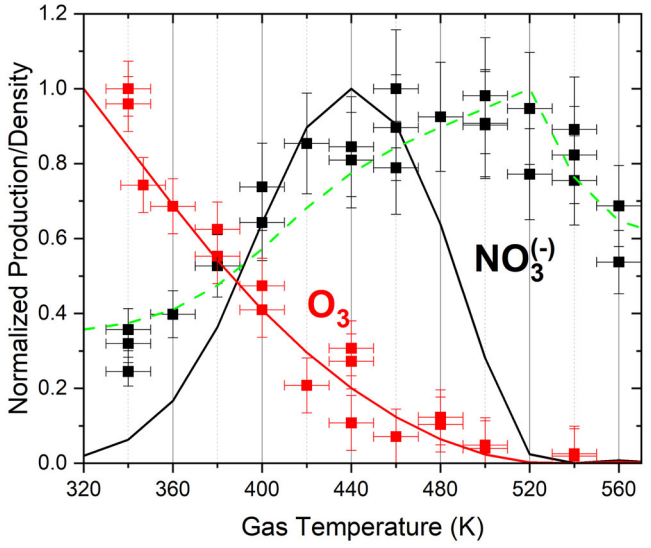

FIGURE 8 | Normalized comparison of the 0D model (lines) and experimental (squares) results. Each data set is normalized respectively. The modeled results are intended to correlate to the densities of the plasma effluent upon reaching the liquid interface, which corresponds to the measured ozone density. The measured nitrate density is in the liquid, post-treatment. The green dotted line is the weighted combination of NO, NO_2, NO_3, N_2O_3, and N_2O_5. The weighting here is arbitrary and only intended to provide an example for how these species may contribute to the observed trend in nitrate production.

3.2 | Chemistry Model Results and Comparison

Good quantitative agreement between the model and experiment was achieved for ozone, with the modeled results having a similar maximum of 6.5×10^{17} cm^{-3} and similar trend, as seen in Figure 8. However, nitrate is not as comparable. At lower temperatures, the nitrate density roughly trends with production until it peaks at 440 K. At which point it sharply decreases, at a much lower temperature than its experimental counterpart. Additionally, the density is much lower than what would be required experimentally, with a maximum of 7.7×10^{14} cm^{-3}. For comparison, to achieve an average production rate of 1 mg/min, with an airflow rate of 1000 sccm, an average density of nitrate in the effluent of at least 9.7×10^{15} cm^{-3} would be required.

This discrepancy is unsurprising as the model fails to take into account the liquid phase chemistry of the numerous RONS which would contribute to the aqueous nitrate density. NO,NO_2, N_2O, N_2O_3, and N_2O_5 can all potentially contribute to the nitrate density in the liquid [32]. See the supplementary materials for a list of relevant liquid reactions. Nitrite, nitric oxide, and nitrous oxide have very low Henry's law constants, meaning they will not uptake into the liquid as well as the other listed species, see Table 2 [47]. Therefore they are much more likely to achieve saturation in the liquid—should their generation outpace their rate of conversion to nitrate—and harshly reduce their diffusion into it. Nitrous oxide is unlikely to convert, as it is an already long-lived species [32].

We can still attempt to estimate these other RONS contributions to the liquid density of nitrate. One potential way this may effect the results is demonstrated in Figure 8 by the green line. This fits much better with our measured values and achieves a more realistic peak density of 4.08×10^{15} cm^{-3}. This fit is obtained via the weighted sum of the species densities:

$$NO_3 + NO_2 + NO \times 10\% + 2 \times N_2O_3 + 2 \times N_2O_5 \times 10\% + N_2\,O \times 1\% \quad (5)$$

TABLE 2 | Relevant Henry's Law Constants [47].

Species	h
O_2	3.24×10^{-2}
O_3	3.00×10^{-1}
N_2	1.6×10^{-2}
N_2O_3	6.00×10^{2}
N_2O_4	3.69×10^{1}
N_2O_5	4.85×10^{1}
N_2O	5.99×10^{-1}
NO	4.40×10^{-2}
NO_2	2.80×10^{-1}
NO_3	4.15×10^{1}

This weighting scheme is largely arbitrary; however, it is loosely based on their relative Henry's law constants and the aqueous reactions listed in the supplementary materials.

3.2.1 | Gas Temperature Influence

Nitrogen fixation in the treated water (the production of aqueous nitrate) is entirely predicated on the formation of RONS in the gas phase. Which RONS are produced, and in what proportions, explicitly influence the formation of aqueous nitrate. It is therefore keenly important to understand the

reactions and mechanisms responsible for the formation of these species in the effluent, to optimize their generation and transport to the liquid. From the modeled results, it is clear the gas temperature within our range has a significant impact on the resultant chemistry. These gas temperature-based shifts in RONS merit some discussion.

The first, and most straightforward effect is observed in ozone. Ozone is a largely undesired product towards the goal of nitrogen fixation. In the post-filament effluent, ozone is largely stable and unlikely to contribute to the density of aqueous nitrate. It is a known greenhouse gas with a low propensity for absorbing into the treated liquid Table 3.

In our model, atomic oxygen is the biggest source of ozone, accounting for over 99% of total formation, irrespective of gas temperature (R1), and simultaneously one of the biggest quenchers of ozone (R2). Ozone formation decreases with increasing temperature, while destruction increases, resulting in the logarithmic decay observed in Figure 8. This suggests prioritizing higher gas temperatures, to avoid the production of ozone; however, it can also be observed in the figure that this begins to negatively impact the production of nitrate.

Nitrate, being the desired product, is most commonly the end result of successive oxidation of nitrogen atoms. Initially, nitric oxide is formed (R3-5), which oxidizes to nitrite (R6-7), and finally nitrate (R8). Further interactions with atomic oxygen can revert nitrate back to nitrite (R9). Above 520 K R9 becomes dominant over R8, resulting in the shift in chemistry present above this temperature.

Nitrite and nitrate form an equilibrium with the larger species, N_2O_5 (R10-11), with this equilibrium being defined by the gas temperature. At low gas temperature ($\lesssim 360$ K) N_2O_5 acts as a storing mechanism for nitrate, protecting it from dissociative

TABLE 3 | Key 0D Model Reactions.

#	Reaction	Rate Constant	Source
R1	$O_g + O_{2g} + M_g \longrightarrow O_{3g} + M_g$	$3.4 \times 10^{-34} \times \left(\frac{300}{T_g}\right)^{1.2} \text{cm}^6\ \text{s}^{-1}$	[35]
R2	$O_g + O_{3g} \longrightarrow O_{2g} + O_{2g}$	$8 \times 10^{-12} \times e^{\frac{-2060}{T_g}} \text{cm}^3\text{s}^{-1}$	[35]
R3	$O_g + NO_g + M_g \longrightarrow NO_g + M_g$	$6.3 \times 10^{-33} \times \left(\frac{140}{T_g}\right)$	[35]
R4	$O_{2g} + N(\,^2D)_g \longrightarrow NO_g + O(\,^1D)_g$	$6 \times 10^{-12} \times \left(\frac{300}{T_g}\right)^{-0.5}$	[36]
R5	$O_g + N_2\left(A\,^3\Sigma_u^+\right)_g \longrightarrow NO_g + N_g$	7×10^{-12}	[36]
R6	$O_g + NO_g + M_g \longrightarrow NO_{2g} + M_g$	$1 \times 10^{-31} \times \left(\frac{300}{T_g}\right)^{1.6}$	[35]
R7	$O_g^- + NO_g^+ + M_g \longrightarrow NO_{2g} + M_g$	$2 \times 10^{-25} \times \left(\frac{300}{T_g}\right)^{2.5}$	[38]
R8	$O_g + NO_{2g} + M_g \longrightarrow NO_{3g} + M_g$	$9 \times 10^{-32} \times \left(\frac{300}{T_g}\right)^{2} \text{cm}^6\ \text{s}^{-1}$	[35]
R9	$O_g + NO_{3g} \longrightarrow O_{2g} + NO_{2g}$	$1.7 \times 10^{-11} \text{cm}^3\ \text{s}^{-1}$	[36]
R10	$N_2O_{5g} + M_g \longrightarrow NO_{3g} + NO_{2g} + M_g$	$1.33 \times 10^{-3} \times \left(\frac{300}{T_g}\right)^{3.5} \times e^{\frac{-11000}{T_g}}\ \text{cm}^3\ \text{s}^{-1}$	[35]
R11	$NO_{2g} + NO_{3g} + A_g \longrightarrow N_2O_{5g} + A_g$	$A = N_2: 2.8 \times 10^{-30} \times \left(\frac{300}{T_g}\right)^{3.5}\ \text{cm}^6\ \text{s}^{-1}$	[36]
		$A = O_2: 2.8 \times 10^{-30} \times \left(\frac{300}{T_g}\right)^{3.5}\ \text{cm}^6\text{s}^{-1}$	
		$A = O_3: 6.0 \times 10^{-30} \times \left(\frac{300}{T_g}\right)^{3.5}\ \text{cm}^6\ \text{s}^{-1}$	
R12	$O_{3g} + NO_{3g} \longrightarrow NO_{2g} + O_{2g} + O_{2g}$	$1.0 \times 10^{-17}\ \text{cm}^3\ \text{s}^{-1}$	[36]
R13	$NO_g + NO_{2g} \longrightarrow N_2O_{3g}$	$7.9 \times 10^{-12} \times \left(\frac{300}{T_g}\right)^{-1.4}\ \text{cm}^3\ \text{s}^{-1}$	[36]
R14	$NO_g + NO_{2g} + A_g \longrightarrow N_2O_{3g} + A_g$	$A = N_2: 3.1 \times 10^{-34} \times \left(\frac{300}{T_g}\right)^{7.7}\ \text{cm}^6\ \text{s}^{-1}$	[36]
		$A = O_2: 3.1 \times 10^{-34} \times \left(\frac{300}{T_g}\right)^{7.7}\ \text{cm}^6\ \text{s}^{-1}$	
		$A = O_3: 6.1 \times 10^{-34} \times \left(\frac{300}{T_g}\right)^{7.7}\ \text{cm}^6\ \text{s}^{-1}$	

reactions with oxygen (R9), ozone (R12), and nitric oxide (R13). This, combined with its high Henry's Law constant and propensity to return to nitrate in the liquid, makes N_2O_5 the ideal effluent product. However, the temperatures at which the formation of N_2O_5 is preferred, simultaneously lack the formation of the prerequisite nitrite and nitrate, resulting in the lower overall production observed at these temperatures (Figure 8).

As temperature increases, so too does the available nitrogen and oxygen, causing a general increase in RONS—this trend is most noticeable in nitrite and nitrate. But as R9 continues to increase with increasing temperature, the nitrate density decreases to eventual irrelevance. The disappearance of N_2O_5 precedes nitrate, due to the lack of its reactant. Nitric oxide and N_2O_3 replace them, with N_2O_3 forming a new equilibrium with nitric oxide and nitrite (R13-14). This RONS regime—observable at 540–560 K in Figure 9—results in decreased nitrate production due to the low Henry's Law constants of nitric oxide and nitrite. N_2O_3, similar to N_2O_5, uptakes into the liquid well and is likely to convert to nitrite/nitrate once absorbed. Despite the abundance of reactants, the high gas temperature prevents N_2O_3 from achieving higher densities.

4 | Conclusion

A water-treating dielectric barrier discharge plasma device was designed in an effort to optimize nitrogen fixation via nitrate for agricultural applications, considering optimization of the generation as well as the transport of species. Current-voltage measurements were used in conjunction with a simplified circuit model to calculate the total deposited power, number of plasma filaments, and average power deposited per filament. OES spectra were compared with numerical simulations to determine the gas temperature in the plasma volume. Optical absorption spectroscopy was used on the plasma effluent to measure ozone density. OAS was also performed on the water to determine the concentration of nitrate in the treated liquid.

The plasma parameters (gas temperature, filament power, geometry, and feed gas) were used to inform a 0D chemistry model. The resulting RONS densities are compared to those measured experimentally, with good agreement between the ozone results. The nitrate comparison is less direct; however, it can likely be rectified by an extension of the model to include a liquid phase. Given the complex interaction between the plasma effluent bubbles and the treated water, a more rigorous 1D model may be required to sufficiently capture the diffusion of the species.

The reaction pathways leading to shifts in the chemistry observed in the 0D model were investigated. Nitrate production in the liquid is observed to maximize when gas temperature favors the formation of N_2O_5 from nitrite and nitrate. This, in effect, stores nitrate as N_2O_5 allowing for a higher collective density and increased production. As temperature continues to increase, N_2O_5 becomes less stable, dampening this "storing" effect. At the highest temperatures, nitrate is reverted to nitrite by atomic oxygen, resulting in a nitric oxide/nitrite/N_2O_5 regime which is less effective at diffusing into the liquid and forming aqueous nitrate.

4.1 | Perspective—Optimizing Nitrate Production

According to the experimental trends (Figure 7) maximum nitrate production in the liquid closely corresponds to its maximum gas phase density observed in the model (Figure 9). This reinforces the obvious conclusion that simply maximizing the gas phase density of nitrate will maximize its transport to the liquid. However, this may hamper the devices ability to achieve higher concentrations of nitrate in the liquid. Once the liquid becomes saturated with nitrate, based on Henry's Law, the gas phase nitrate would no longer diffuse into it, and be lost. This suggests that, to obtain higher concentrations of aqueous nitrate, other species with good liquid diffusion and a high propensity to convert to nitrate should be prioritized, such as N_2O_5 or N_2O_3.

This may be achieved by targeting a higher or lower gas temperature regime (such as by adjusting the applied power), or by adjusting the transport time of the plasma effluent to the liquid, allowing for more (or less) time for the chemistry to evolve into these larger more stable species in the gas phase. Alternatively, this low concentration may not be an issue for in-line

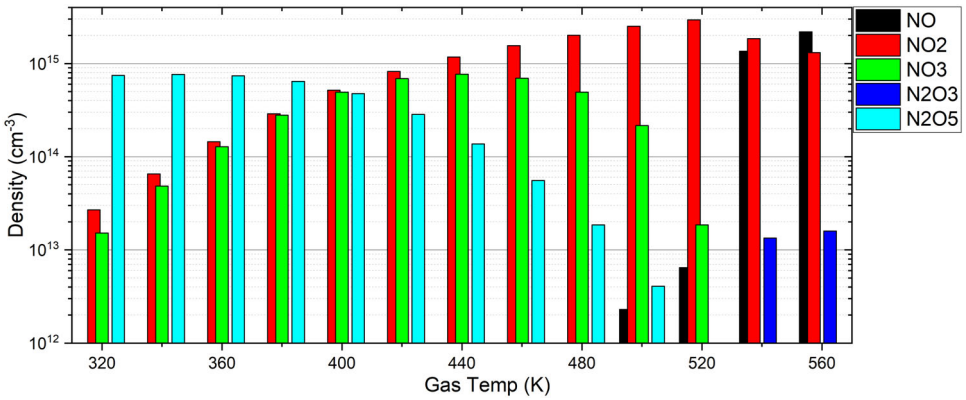

FIGURE 9 | 0D model results of the some of the most significant RONS for generating nitrate in the liquid phase. Densities are taken from the final time step at $t = 0.166$ s. The largest species tend to be favored at lower temperatures. Initially, N_2O_5 is dominant, before transitioning to a nitrate/nitrite regime, then solely nitrite, and finally nitrite/nitric oxide.

fertigation. The treated water could be simultaneously withdrawn and replenished, given some optimal liquid throughput. Or, if high concentrate solution is still desired, distilling methods could be applied to achieve this.

Acknowledgements

This work was partly supported by North Carolina State University's Game-Changing Research Incentive Program for the Plant Sciences Inititative (GRIP4PSI). This material is partly based upon work supported by the U.S. Department of Energy, Office of Science, Office of Fusion Energy Science under Award Number DE-SC0023235 and partly based upon work supported by the National Science Foundation under Grant No. PHY 2107901.

Conflicts of Interest

The authors declare no conflict of interest.

Data Availability Statement

The data that support the findings of this study are openly available in Dryad at https://doi.org/10.5061/dryad.crjdfn3d9.

References

1. L. Lassaletta, G. Billen, B. Grizzetti, J. Anglade, and J. Garnier, "50 Year Trends in Nitrogen Use Efficiency of World Cropping Systems: The Relationship Between Yield and Nitrogen Input to Cropland," *Environmental Research Letters* 9, no. 10 (2014): 105011.

2. T. Javed, I. I, R. K. Singhal, et al., "Recent Advances in Agronomic and Physio-Molecular Approaches for Improving Nitrogen Use Efficiency in Crop Plants," *Frontiers in Plant Science* 13 (2022): 877544.

3. G. Billen, J. Garnier, and L. Lassaletta, "The Nitrogen Cascade From Agricultural Soils to the Sea: Modelling Nitrogen Transfers at Regional Watershed and Global Scales," *Philosophical Transactions of the Royal Society B: Biological Sciences* 368, no. 1621 (2013): 20130123.

4. M. A. Sutton, A. Bleeker, C. M. Howard, et al., *Our Nutrient World. The Challenge to Produce More Food & Energy With Less Pollution* (Centre for Ecology & Hydrology, 2013).

5. P. Ranieri, N. Sponsel, J. Kizer, et al., "Plasma Agriculture: Review From the Perspective of the Plant and Its Ecosystem," *Plasma Processes and Polymers* 18, no. 1 (2020): 2000162, https://doi.org/10.1002/ppap.202000162.

6. Z. Shen, " Liquid Nitrate Fertilizer Production With Various Atmospheric Pressure Discharges," PhD thesis. Purdue University, 2019.

7. A. Lindsay, B. Byrns, W. King, et al., "Fertilization of Radishes, Tomatoes, and Marigolds Using a Large-Volume Atmospheric Glow Discharge," *Plasma Chemistry and Plasma Processing* 34 (2014): 1271–1290.

8. D. P. Park, K. Davis, S. Gilani, et al., "Reactive Nitrogen Species Produced in Water by Non-Equilibrium Plasma Increase Plant Growth Rate and Nutritional Yield," *Current Applied Physics* 13 (2013): S19–S29.

9. S. Ruamrungsri, C. Sawangrat, K. Panjama, et al., "Effects of Using Plasma-Activated Water as a Nitrate Source on the Growth and Nutritional Quality of Hydroponically Grown Green Oak Lettuces," *Horticulturae* 9, no. 2 (2023): 248.

10. K. Tachibana and T. Nakamura, "Comparative Study of Discharge Schemes for Production Rates and Ratios of Reactive Oxygen and Nitrogen Species in Plasma Activated Water," *Journal of Physics D: Applied Physics* 52, no. 38 (2019): 385202.

11. C. Robinson and K. Stapelmann, "Plasma Treating Water for Nitrate Based Nitrogen Fertilizer - A Review of Recent Device Designs," *Current Opinion in Green and Sustainable Chemistry* 50 (2024): 100978.

12. R. Laurita, D. Barbieri, M. Gherardi, V. Colombo, and P. Lukes, "Chemical Analysis of Reactive Species and Antimicrobial Activity of Water Treated by Nanosecond Pulsed DBD Air Plasma," *Clinical Plasma Medicine* 3, no. 2 (2015): 53–61.

13. A. L. V. Cubas, F. M. Ferreira, D. B. Gonçalves, d. M. Medeiros Machado, N. A. Debacher, and E. H. S. Moecke, "Influence of Non-Thermal Plasma Reactor Geometry and Plasma Gas on the Inactivation of *Escherichia Coli* in Water," *Chemosphere* 277 (2021): 130255.

14. V. Rathore, D. Patel, S. Butani, and S. K. Nema, "Investigation of Physicochemical Properties of Plasma Activated Water and Its Bactericidal Efficacy," *Plasma Chemistry and Plasma Processing* 41 (2021): 871–902.

15. C. Y. Hou, Y. C. Lai, C. P. Hsiao, et al., "Antibacterial Activity and the Physicochemical Characteristics of Plasma Activated Water on Tomato Surfaces," *Lwt - Food Science and Technology* 149 (2021): 111879.

16. Q. Xiang, C. Kang, L. Niu, D. Zhao, K. Li, and Y. Bai, "Antibacterial Activity and a Membrane Damage Mechanism of Plasma-Activated Water Against Pseudomonas Deceptionensis Cm2," *Lwt* 96 (2018): 395–401.

17. C. M. Lin, C. P. Hsiao, H. S. Lin, et al., "The Antibacterial Efficacy and Mechanism of Plasma-Activated Water against Salmonella Enteritidis (ATCC 13076) on Shell Eggs," *Foods* 9, no. 10 (2020): 1491.

18. B. Myers, E. Barnat, and K. Stapelmann, "Atomic Oxygen Density Determination in the Effluent of the COST Reference Source Using in Situ Effective Lifetime Measurements in the Presence of a Liquid Interface," *Journal of Physics D: Applied Physics* 54, no. 45 (2021): 455202.

19. K. Stapelmann, B. Myers, M. H. Quesada, E. Lenker, and P. J. Ranieri, "Following O and OH in He/O2 and He/H2O Gas Mixtures-Ṫ From the Gas Phase Through the Liquid Phase to Modifications on a Biological Sample," *Journal of Physics D: Applied Physics* 54, no. 43 (2021): 434003.

20. K. Hadinoto, J. B. Astorga, H. Masood, et al., "Efficacy Optimization of Plasma-Activated Water for Food Sanitization Through Two Reactor Design Configurations," *Innovative Food Science & Emerging Technologies* 74 (2021): 102867.

21. J. Sun, D. Alam, R. Daiyan, et al., "A Hybrid Plasma Electrocatalytic Process for Sustainable Ammonia Production," *Energy & Environmental Science* 14, no. 2 (2021): 865–872.

22. K. Hadinoto, N. Rao, J. B. Astorga, et al., "Hybrid Plasma Discharges for Energy-Efficient Production of Plasma-Activated Water," *Chemical Engineering Journal* 451 (2023): 138643.

23. A. Mai-Prochnow, D. Alam, R. Zhou, T. Zhang, K. Ostrikov, and P. J. Cullen, "Microbial Decontamination of Chicken Using Atmospheric Plasma Bubbles," *Plasma Processes and Polymers* 18, no. 1 (2021): 2000052.

24. A. D. Lindsay, D. B. Graves, and S. C. Shannon, "Fully Coupled Simulation of the Plasma Liquid Interface and Interfacial Coefficient Effects," *Journal of Physics D: Applied Physics* 49, no. 23 (2016): 235204, https://doi.org/10.1088/0022-3727/49/23/235204.

25. S. Liu and M. Neiger, "Electrical Modelling of Homogeneous Dielectric Barrier Discharges Under an Arbitrary Excitation Voltage," *Journal of Physics D: Applied Physics* 36, no. 24 (2003): 3144.

26. P. J. Bruggeman, N. Sadeghi, D. Schram, and V. Linss, "Gas Temperature Determination From Rotational Lines in Non-Equilibrium Plasmas: A Review," *Plasma Sources Science and Technology* 23, no. 2 (2014): 023001.

27. N. Bibinov, H. Halfmann, P. Awakowicz, and K. Wiesemann, "Relative and Absolute Intensity Calibrations of a Modern Broadband Echelle Spectrometer," *Measurement Science and Technology* 18, no. 5 (2007): 1327.

28. V. Gorshelev, A. Serdyuchenko, M. Weber, W. Chehade, and J. Burrows, "High Spectral Resolution Ozone Absorption Cross-Sections-Part 1: Measurements, Data Analysis and Comparison With Previous Measurements Around 293 K," *Atmospheric Measurement Techniques* 7, no. 2 (2014): 609–624.

29. P. Lukes, E. Dolezalova, I. Sisrova, and M. Clupek, "Aqueous-Phase Chemistry and Bactericidal Effects From an Air Discharge Plasma in Contact With Water: Evidence for the Formation of Peroxynitrite through a Pseudo-Second-Order Post-Discharge Reaction of H2O2 and HNO2," *Plasma Sources Science and Technology* 23, no. 1 (2014): 015019.

30. M. J. Traylor, M. J. Pavlovich, S. Karim, et al., "Long-Term Antibacterial Efficacy of Air Plasma-Activated Water," *Journal of Physics D: Applied Physics* 44, no. 47 (2011): 472001.

31. C. Verlackt, W. Van Boxem, and A. Bogaerts, "Transport and Accumulation of Plasma Generated Species in Aqueous Solution," *Physical Chemistry Chemical Physics* 20, no. 10 (2018): 6845–6859.

32. A. M. Lietz and M. J. Kushner, "Air Plasma Treatment of Liquid Covered Tissue: Long Timescale Chemistry," *Journal of Physics D: Applied Physics* 49, no. 42 (2016): 425204.

33. G. Giudicelli, A. Lindsay, L. Harbour, et al., " 3.0 - MOOSE: Enabling Massively Parallel Multiphysics Simulations," *SoftwareX* 26 (2024): 101690, https://doi.org/10.1016/j.softx.2024.101690.

34. C. DeChant, C. Icenhour, S. Keniley, et al., "Verification and Validation of the Open-Source Plasma Fluid Code: Zapdos," *Computer Physics Communications* 291 (2023): 108837.

35. Y. Sakiyama, D. B. Graves, H. W. Chang, T. Shimizu, and G. E. Morfill, "Plasma Chemistry Model of Surface Microdischarge in Humid Air and Dynamics of Reactive Neutral Species," *Journal of Physics D: Applied Physics* 45, no. 42 (2012): 425201.

36. W. Van Gaens and A. Bogaerts, "Kinetic Modelling for an Atmospheric Pressure Argon Plasma Jet in Humid Air," *Journal of Physics D: Applied Physics* 46, no. 27 (2013): 275201.

37. A. Phelps URL: ftp://jila.colorado.edu/collision_data.

38. I. Kossyi, A. Y. Kostinsky, A. Matveyev, and V. Silakov, "Kinetic Scheme of the Non-Equilibrium Discharge in Nitrogen-Oxygen Mixtures," *Plasma Sources Science and Technology* 1, no. 3 (1992): 207.

39. M. Brabant, A. Demaude, J. Mertens, et al., "New Perspectives of Atmospheric Pressure Dielectric Barrier Discharges for the Deposition of Thin Films: From Uncontrolled Amorphous Plasma-Polymer Layers to Chemically Patterned and Crystalline (in) Organic Coatings," *Surface and Coatings Technology* 495 (2025): 131559.

40. R. Wang, Y. Yang, S. Chen, H. Jiang, and P. Martin, "Power Calculation of Pulse Power-Driven DBD Plasma," *IEEE Transactions on Plasma Science* 49, no. 7 (2021): 2210–2216.

41. F. Rodrigues, J. Pascoa, and M. Trancossi, "Heat Generation Mechanisms of Dbd Plasma Actuators," *Experimental Thermal and Fluid Science* 90 (2018): 55–65.

42. D. Ashpis, M. Laun, and E. Griebeler, " Progress Toward Accurate Measurements of Power Consumption of DBD Plasma Actuators," in *50th AIAA aerospace sciences meeting including the new horizons forum and aerospace exposition* 2012: 823.

43. M. Babaie, P. Davari, F. Zare, et al., "Effect of Pulsed Power on Particle Matter in Diesel Engine Exhaust Using a DBD Plasma Reactor," *IEEE Transactions on Plasma Science* 41, no. 8 (2013): 2349–2358.

44. F. Kogelheide, B. Offerhaus, N. Bibinov, et al., "Characterisation of Volume and Surface Dielectric Barrier Discharges in N2-O2 Mixtures Using Optical Emission Spectroscopy," *Plasma Processes and Polymers* 17, no. 6 (2020): 1900126.

45. B. Offerhaus, J. W. Lackmann, F. Kogelheide, et al., "Spatially Resolved Measurements of the Physical Plasma Parameters and the Chemical Modifications in a Twin Surface Dielectric Barrier Discharge for Gas Flow Purification," *Plasma Processes and Polymers* 14, no. 10 (2017): 1600255.

46. U. Kogelschatz and P. Baessler, " Determination of Nitrous Oxide and Dinitrogen Pentoxide Concentrations in the Output of Air-Fed Ozone Generators of High Power Density," *Ozone: Science & Engineering* 9, no. 3 (1987): 195–206.

47. R. Sander, "Compilation of Henry's Law Constants (Version 4.0) for Water as Solvent," *Atmospheric Chemistry and Physics* 15, no. 8 (2015): 4399–4981.

Supporting Information

Additional supporting information can be found online in the Supporting Information section.